Intracavity Laser Spectroscopy with Fourier-Transform Detection of Tungsten Sulfide, WS: Analysis of the (1,0) band of the [13.10] Ω=1 – $X\,^3\Sigma^-_{0^+}$ transition

Jack C. Harms,[a] Brendan M. Ratay,[a] Kristin N. Bales, [a] James J. O'Brien,[a] and Leah C. O'Brien[b]

[a]*Department of Chemistry and Biochemistry, University of Missouri-St. Louis, Saint Louis, MO 63121, USA*

[b]*Department of Chemistry, Southern Illinois University Edwardsville, Edwardsville, IL 62026, USA*

Abstract

The (1,0) band of the [13.10] Ω=1 – $X\,^3\Sigma^-_{0^+}$ transition of WS has been observed and recorded at Doppler-limited resolution using intracavity laser absorption spectroscopy detected with a Fourier-transform spectrometer (ILS-FTS). The tungsten sulfide molecules were produced in the plasma discharge formed when 0.35 A of RF current were applied to a W-lined Cu hollow cathode in an atmosphere that was 0.1% CS_2, ~30% H_2, and ~70% Ar at a total pressure of 1 torr. The hollow cathode was located within the resonator cavity of a tunable Ti:Sapphire laser, causing molecular absorption to be superimposed upon the broadband profile of the laser. This profile was detected using a Bruker IFS 125M spectrometer using an instrument resolution of 0.01 cm^{-1}. The ILS-FTS spectrum was analyzed using PGOPHER. Experimental line positions from the laser induced fluorescence (LIF) spectrum of WS [Tsang *et al.*, *J. Mol. Spec.*, **359**, 31 (2019)] were included in the fit, and a limited Dunham model was built in PGOPHER to characterize the $X\,^3\Sigma^-_{0^+}$ ground state of WS. The rotational coverage of the ground state is expanded from 0<J<35 to 0<J<62, the uncertainty in the ground state constants for WS are reduced by a factor of three, and a potential energy curve for that state is produced from the Dunham constants using the RKR method.

Introduction

Diatomic molecules containing 5*d*-transition metals are spectroscopic targets of high fundamental interest. These molecules are difficult to approach from a theoretical standpoint due to the large number of electrons and readily accessible valence orbitals. Additionally, relativistic effects (like spin-orbit coupling) dramatically affect the energetic landscape, often impacting the total energy more significantly than individual components of the electronic angular momentum.[1-2] The magnitude of spin-orbit coupling leads to the mixing of Λ-S states, leading to Hund's case (c) Ω-states. Transitions between Ω-states are often quite generic in appearance, masking their underlying nature with their apparent simplicity. By combining high-level *ab initio* methods with robust experimental observations, these species can be characterized and better understood to the mutual benefit of both avenues of inquiry.

The electronic structure of tungsten sulfide, WS, is of additional interest due to the desirable properties of WS_2 monolayers as semiconducting materials in nanoelectronic devices.[3-4] The electronic structure of the diatomic molecule was first explored by Liang and Andrews[5] in 2002, who used density functional theory (DFT) calculations to interpret vibrational frequencies observed from Group VI metal sulfides matrix-isolated in Ar. While they did not observe WS experimentally, their calculations predicted a $^3\Sigma^-$ ground state for WS from the $\sigma^2\delta^2$ configuration, where the molecular σ-orbital is predominantly a hybridized $6s$-$5d_\sigma$ W orbital and the molecular δ-orbital is entirely W $5d_\delta$. The diatomic molecule did not enter the scientific literature again until 2017 in a special issue of *J. Phys. Chem. A* commemorating the works of Lester Andrews, where Sevy *et al.*[6] reported bond dissociation energies (BDE) for W-diatomics determined by resonant two-photon ionization spectroscopy. They also performed the DFT calculations similar to those of Liang and Andrews[5], expanding the initial inquiry by considering various orbital occupations in their evaluation. The molecular dissociation energy of WS was determined to by 39800±25 cm^{-1} (4.953±0.003 eV), and their computational results agreed with the assignment of a $^3\Sigma^-$ ground state arising from orbitals that are largely W $6s$ and $5d$ in character.

The most comprehensive investigation of diatomic WS was reported in 2019 by Tsang *et al.*[1] using a combination of *ab initio* and experimental methods. They observed 14 rotationally resolved vibrational bands of WS in the near-IR using laser induced fluorescence (LIF). These bands were assigned to 6 different electronic transitions originating from both spin-orbit components of the $^3\Sigma^-$ ground state. Transitions due to the four most naturally abundant isotopologues of WS were observed and rotationally analyzed ($^{182}W^{32}S$ 25.16%, $^{183}W^{32}S$ 13.58%, $^{184}W^{32}S$ 29.09%, and $^{186}W^{32}S$ 26.99%). The spectra were interpreted with assistance from high level *ab initio* calculations: state-averaged complete active space self-consistent field (SA-CASSCF) followed by multi-reference configuration interaction with single and double excitation plus Davidson's correction (MRCISD+Q), using the state-interaction (SI) method to calculate the spin-orbit matrix. These calculations predict a separation of 2258 cm^{-1} between the spin-orbit components of the $^3\Sigma^-$ ground state, but the exact value could not be determined experimentally because a common excited state connecting the two components was not observed. Recently, Zhang *et al.*[7] measured this separation to be 2181.10±0.09 cm^{-1} using LIF and single-vibronic level (SVL) emission spectroscopies, supporting the preliminary value of 2181.152±0.002 cm^{-1} reported by our group at the 74th International Symposium on Molecular Spectroscopy.[8]

In this study, the spectroscopic characterization of the electronic spectrum of WS has been expanded using intracavity laser absorption spectroscopy detected with a Bruker IFS 125 M

Fourier-transform spectrometer (ILS-FTS). The (1,0) band of the [13.10] $\Omega=1 - X\,^3\Sigma^-_{0^+}$ transition of WS has been observed and recorded at Doppler-limited resolution. Rotational branches for $^{182}W^{32}S$, $^{183}W^{32}S$, $^{184}W^{32}S$, and $^{186}W^{32}S$ were resolved and identified. Line positions for the (0,0), (0,1), and (0,2) bands of the [13.10] $\Omega=1 - X\,^3\Sigma^-_{0^+}$ and the (1,0), (0,0), and (0,1) bands of the [12.37] $\Omega=1 - X\,^3\Sigma^-_{0^+}$ transitions of WS reported by Tsang *et al.*[1] were included with the ILS-FTS data in a PGOPHER[9] fit of the data. The ground state was fit to a mass-dependent Dunham[10] model (each isotopologue treated separately) using the constrained-variables approach introduced by Brier and coauthors[11-12], and the vibrational levels of the excited states were treated individually. The obtained Dunham constants were used to produce a potential energy curve for the $\Omega=0^+$ component of the $^3\Sigma^-$ ground state using the Rydberg-Klein-Rees (RKR) method.

Experimental Methods

The ILS-FTS spectra were collected using the system at the University of Missouri – St. Louis (UMSL), which has been described in detail elsewhere.[13] A schematic of the combined instrument is provided in Figure 1. ILS-FTS operation requires synchronization of the two time-dependent methods. The ILS method requires that the output of the laser be examined at a particular evolution time of the laser, which is controlled by an acousto-optic modulator (AOM1). AOM1 initiates and terminates the ILS cycle by altering the intensity of a Coherent Verdi™ V-10 pump laser that is directed into the laser medium. This pump laser is used to drive either a dye laser[13] or a Ti:Sapphire laser, providing tunable output over the 11,000-18,000 cm^{-1} region. The ILS output is directed into a Bruker IFS 125 M Fourier-transform spectrometer with a maximum instrument resolution of 0.0035 cm^{-1}. The FT-spectrometer samples the interferogram in 5 µsec intervals after each detected zero-crossing from the internal He-Ne calibration laser. For synchronous ILS-FTS operation, these zero-crossings are detected using a National Instruments PXI-7841R field programmable gate array (FGPA) board contained within a NI PXI-1033 chasis and programmed

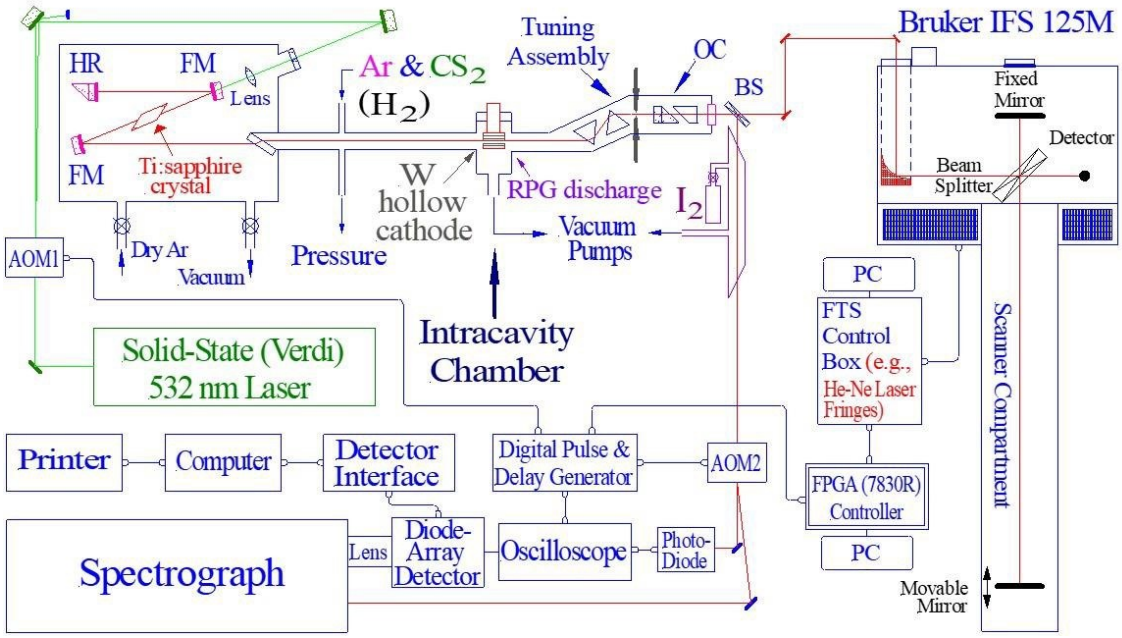

Figure 1: Schematic of the ILS-FTS system at the University of Missouri – St. Louis.

using LabView software. Upon detection of a zero-crossing, a 5 μsec delay is initiated in the LabView program, after which a signal is sent to the AOM1 terminating the ILS cycle by diverting the pump laser into a beam stop. After a sufficient delay (5-10 μsec) to ensure the gain medium falls below the lasing threshold, another signal is sent to the AOM and the pump beam is redirected back into the gain medium, reinitiating the laser cycle.

The target molecules are produced in the plasma discharge from a hollow cathode located within the resonator cavity of the ILS laser. As a result, molecular absorption is enhanced by laser action in the time between laser initiation and the FTS sampling window (termed the generation time, t_g). The FTS interferogram may be scanned at 5, 7.5, 10, or 15 kHz using a fast Si-diode detector, corresponding to zero-crossings every 100, 75, 50, or 33.3 μsec and equivalent t_g values of 85, 55, 40, and 25 μsec, respectively. The effective pathlength, L_{eff}, for ILS measurements is given by

$$L_{eff} = t_g c \left(\frac{l}{L}\right) \quad (1)$$

where c is the speed of light, l is the distance in the resonator cavity occupied by the absorber (the length of the hollow cathode) and L is the total length of the resonator cavity.

For this study, WS molecules were produced in the plasma discharge formed when 0.35 A of RF-pulsed (~125 kHz) DC current from an ENI RPG 50 Power Supply (Figure 1) were applied to a W-lined Cu hollow cathode (25 mm long) in an atmosphere that was 0.1% CS_2, ~30% H_2, and ~70% Ar at a total pressure of 1 torr. The RF-pulses are much faster than the ILS cycle, resulting in relatively constant conditions over the course of t_g. Plasma operation was not synchronized to the ILS-FTS duty cycle. By accident, the H_2 initially was included due to a small leak through a closed mass flow controller, but it was found to have a significant impact on signal intensity with WS absorption features being enhanced ~10x by the inclusion of H_2 vs. Ar/CS_2 only. The origin of this benefit is unclear, but it is worth noting that the plasma deposition processes used to produce WS_2 thin films also are enhanced by the inclusion of H_2 as a W-reducing agent in the duty cycle of operation.[3] It also is possible that H_2 participates through a complex mechanism with an SH intermediate, similar to the proposed mechanism involving hydrogen's role in the enhanced formation of PO.[14] An FTS scan rate of 5 kHz was utilized for these measurements, resulting in a t_g of 85 μsec and an L_{eff} of 300 m for the species produced within the 2.1 m resonator cavity of the Ti:Sapphire laser. Ten individual scans with an instrumental resolution of 0.01 cm^{-1} were collected and co-added for this analysis, resulting in a total collection time of 100 minutes (10 minutes/scan).

The ILS-FTS spectra are processed to a useable form with PGOPHER.[9] The Baseline/Peaks dialogue window is used to apply a local baseline to the broadband profile of the ILS signal (Baseline Settings: Baseline Window = 1000; Noise Level = 2.0; Noise Window = 200; Inverse, Dense, and Local settings selected for a Smooth baseline) and an absorbance spectrum is produced. The spectra are calibrated using the appropriate function in PGOPHER[9]: atomic lines due to Ar (I) are identified and used to apply an absolute correction to the wavenumber position of the spectral features using the line positions reported by Kerber *et al.*[15] Agreement between observed Ar lines and reported wavelengths was ±0.003 cm^{-1} after calibration, with an expected internal precision of 0.01 cm^{-1} for the FT-spectrometer. A portion of the (1,0) band of the [13.10] $\Omega=1 - X\,^3\Sigma^-_{0^+}$ transition of WS is provided in Figure 2. The entire ILS-FTS spectrum analyzed in this work is provided as a text file in the Supplementary Materials.

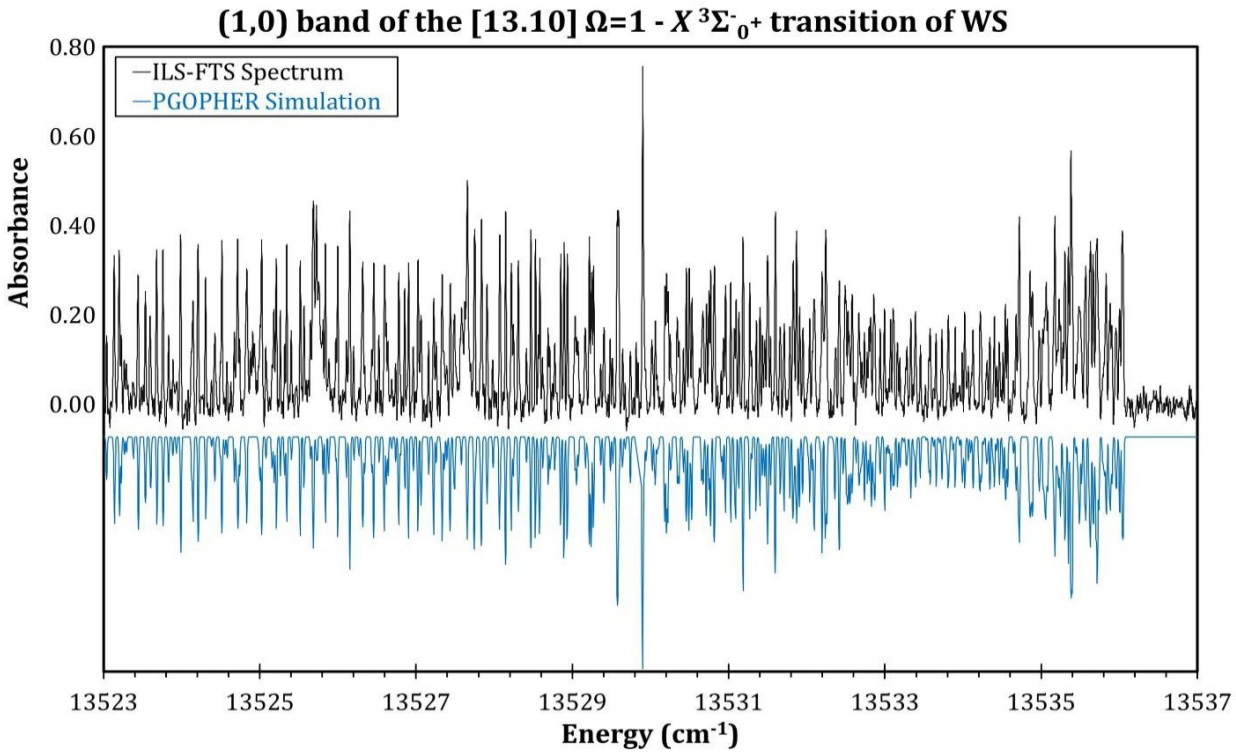

Figure 2: The ILS-FTS spectrum of the (1,0) band of the [13.10] Ω=1 – $X\,^3\Sigma^-_{0^+}$ transition of WS. The PGOPHER[9] simulation (T=300 K, Gaussian Line Width=0.015 cm^{-1}) of the transition is inverted and displayed in blue in the lower portion of the figure. The vibrational shift between isotopologues can be identified by the three intense (and one weak) bandheads at the right side of the figure at approximately 13,535.4, 13535.8, and 13536.2 cm^{-1}.

Results and Analysis

A red-degraded band was observed at Doppler-Limited resolution in the near-infrared using ILS-FTS. The band is characterized by three dominant bandheads near 13,536 cm^{-1}. Three branch patterns are readily observed, each consisting of 4 isotopologue components. The three branch patterns were consistent with a P-, Q- and R-branch, with the Q-branch being the most intense and the P-branch being the weakest. The four isotopologue components consisted of three-equally spaced and equally intense features, with the fourth component roughly half as intense and spaced halfway between the two components of higher energy. These relative intensities are consistent with the relative abundances of the naturally occurring isotopes of tungsten (^{182}W 26.50%, ^{183}W 14.31%, ^{184}W 30.64%, ^{186}W 28.43%), with the lighter molecular isotopologues shifted further to the blue in the spectra. The rotational spacing (illustrated in Figure 3) was consistent with the rotational constants reported by Tsang *et al.*[1] for WS, and the separation between the isotopologues was 0.4 cm^{-1}, marking the transition as Δv=+1. A rotational analysis confirmed the identity of the lower state of the transition as the $X\,^3\Sigma^-_{0^+}$ ground state of WS using combination differences with the reported line positions from Tsang *et al.*[1] The transition was fit band-by-band using PGOPHER[9] to determine the rotational constants for both states. The resulting *B*-values were consistent with those of v=0 for the [13.10] Ω=1 state of Tsang *et al.*[1], and separation between this state and the

observed excited state (431 cm^{-1}) is consistent with the $\Delta G_{1/2}$ values observed and calculated for WS by Tsang *et al.*[1] As a result, the observed band was assigned as the (1,0) band of the [13.10] Ω=1 – $X\,^3\Sigma^-_{0^+}$ transition of WS.

The quality of the ILS-FTS spectra with clear isotopic resolution and broad rotational coverage (0<J″<62) provided in this work along with the wealth of experimental data generously provided in the Supplementary Materials of Tsang *et al.*[1] encouraged a Dunham[10] analysis of the $X\,^3\Sigma^-_{0^+}$ ground state of WS. A Dunham[10] model is useful for several reasons: the potential for parameter reduction; the ease in predicting the energies of unobserved vibrational states; and the ability to produce an electronic potential surface from those predicted vibrational energies. To perform the Dunham[10] analysis, the 655 ILS-FTS line positions for the (1,0) band of the [13.10] Ω=1 – $X\,^3\Sigma^-_{0^+}$ transition were added to the 1104 LIF[1] line positions for the (1,0), (1,1), (0,0), (0,1) bands of the [12.37] Ω=1 – $X\,^3\Sigma^-_{0^+}$ transition and the (0,0), (0,1), and (0,2) bands of the [13.10] Ω=1 – $X\,^3\Sigma^-_{0^+}$ transition, and a Dunham model was built into PGOPHER[9] using the constrained-variables approach first implemented by Breier and coworkers[11,12] and used by our group.[16-18] This approach incorporates the Dunham parameters (Y_{10}, Y_{01}, Y_{02} etc.) as PGOPHER Variables.[19] These new Variables[19] are then used to define the band-by-band parameters (Origin, B, D, etc.) using PGOPHER[9] Constraints[20] and the appropriate Dunham[10] relationships [$B_v=Y_{01}+Y_{11}(v+1/2)+Y_{21}(v+1/2)^2$…]. The initial lines of the PGOPHER[9] input file (see Supplementary Materials) contain the equations and format used to define the constrained variables.[20]

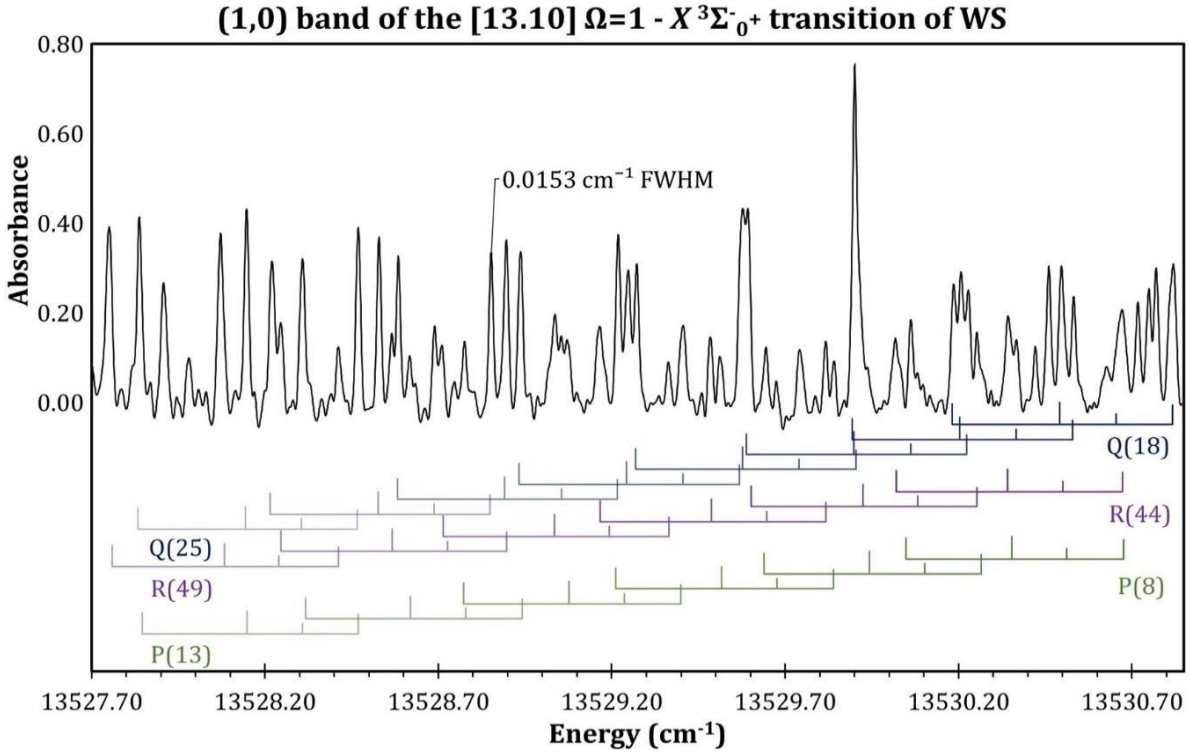

Figure 3: A small portion of the ILS-FTS spectrum of the (1,0) band of the [13.10] Ω=1 – $X\,^3\Sigma^-_{0^+}$ transition of WS. The rotational branches are identified as isotopic clusters (from Left to Right: $^{186}W^{32}S$, $^{184}W^{32}S$, $^{183}W^{32}S$, and $^{182}W^{32}S$). The height of the identifying line is consistent with the natural abundance for the tungsten isotopes: 26.50%, 14.31%, 30.64%, and 28.43% for ^{182}W, ^{183}W, ^{184}W, and ^{186}W. The Q(24) line of $^{182}W^{32}S$ is isolated and indicated in the upper trace of the spectrum. The experimental FWHM, is 0.0153 cm^{-1}, consistent with a Doppler temperature of 545 K, which is reasonable for the plasma discharge used to produce the WS molecules.

The (0,0) bands were not isotopically resolved by Tsang *et al.*,[1] requiring the inclusion of the [12.37] Ω=1 – $X\,^3\Sigma^-_{0^+}$ transition for which both the (1,0) and (1,1) bands were detected with isotopic resolution. The ILS-FTS data and LIF data[1] were assigned uncertainties of 0.003 cm^{-1} and 0.02 cm^{-1} in accordance with the absolute uncertainties associated with the respective experimental techniques.

It should be noted that a typographical error was discovered in the 40 pages of line positions reported by Tsang *et al.*[1]: the line positions for R(9) and R(12) of the (0,2) band of the [13.10] Ω=1 – $X\,^3\Sigma^-_{0^+}$ transition of $^{186}W^{32}S$ apparently were not observed in the spectrum, but the J-labeling in the table is continuous. As a result, the R(10) and R(11) lines are reported as R(9) and R(10), and the R(13)-R(23) lines are reported as R(11)-R(21). Additionally, the first two line positions of that branch are duplicated and labeled R(22) and R(23).

Line positions for the (0,2) band of the [13.10] Ω=1 – $X\,^3\Sigma^-_{0^+}$ transition were only reported[1] for $^{186}W^{32}S$, which limited the scope of the Dunham[10] model to $^{186}W^{32}S$. Due to this limitation of the expansive yet minimal data set, a comprehensive mass-independent Dunham analysis[21,22] was not warranted, and thus each isotopologue was treated independently. The three rotationally analyzed vibrational levels of the ground state of $^{186}W^{32}S$ enable the determination of 5 rovibrational constants: Y_{10}, Y_{20}, Y_{01}, Y_{11}, and Y_{21}, which correspond to the conventional terms[23,24] ω_e, $-\omega_e x_e$, B_e, $-\alpha_e$, and γ_e (not to be confused with the spin-rotation constant γ). It was found that the rotational structure of these three vibrational levels was well described using only first two rotational terms (Y_{01} and Y_{11}) and that inclusion of Y_{21} did not improve the quality of the fit. While the LIF transitions (J''_{max}=35) of Tsang *et al.*[1] were well described without treatment of centrifugal distortion, the ILS-FTS data (J''_{max}=62) required the inclusion of Y_{02} (≡$-D_e$) due to the significance of the effect for J″>40. As the ILS-FTS data only connect with v″=0, the vibrational dependence of centrifugal distortion could not be determined in the fit.

The anharmonicity correction to the vibrational energy (Y_{20}) could be determined only for $^{186}W^{32}S$ because of the aforementioned limitation. Mass-scaling was used to estimate the magnitude of this parameter for the other isotopologues of WS, using the general relationship[22]

$$Y_{lm}^{\alpha} = Y_{lm}^{1}\left(\frac{\mu_1}{\mu_\alpha}\right)^{m+l/2} \qquad (2)$$

where l represents the vibrational dependence of the parameter, m represents the rotational dependence of the parameter, μ is the reduced mass of the respective molecules, the 1 superscripts/subscripts represent the reference isotopologue for which the parameter is known ($^{186}W^{32}S$), and the α superscripts/subscripts represent each other isotopologue. In the analysis the Y_{20} parameters for $^{182}W^{32}S$, $^{183}W^{32}S$, and $^{184}W^{32}S$ were constrained to equation (2) in the fit.

The Dunham constants for the $X\,^3\Sigma^-_{0^+}$ state are provided in Table 1. The constants for v=1 of the [13.10] Ω=1 state of WS are provided in Table 2. The root mean squared (RMS) residuals from the PGOPHER[9] fit are provided in Table 3. The individual line positions, assignments, and residuals are provided in Table 4. The Supplementary Materials contain a comparison of the band-by-band constants from Tsang *et al.*[1] (Table S1) and from this study (Table S2) and the PGOPHER[9] .pgo and input files used to perform the fit.

The determined Dunham parameters were used to produce a potential energy curve for $^{186}W^{32}S$ with the RKR method. This approach was

Table 1: Dunham Parameters (in cm^{-1}) for the $X\,^3\Sigma^-_{0^+}$ Ground State of WS. The lower portion of the table compares the ratio between the determined spectroscopic constants for each isotopologue to the expected mass-scaling for the Dunham model [Equation (2)]. Deviations from 1 indicate isotopologue dependent deviations from the Dunham model: the obtained ratios indicate that the Dunham model is reasonably appropriate for this system relative to experimental uncertainty.

	Y_{10}	Y_{20}	Y_{30}	Y_{01}	$Y_{11} \times 10^3$	$Y_{02} \times 10^6$
$^{182}W^{32}S$	560.0289 (94)	-1.4187[a]	-0.00402[a]	0.1453059 (74)	-0.5469 (29)	-0.0392 (22)
$^{183}W^{32}S$	559.8016 (98)	-1.4175[a]	-0.00401[a]	0.1451697 (83)	-0.5731 (33)	-0.0253 (29)
$^{184}W^{32}S$	559.57826 (79)	-1.4163[a]	-0.00401[a]	0.1450513 (54)	-0.5267 (14)	-0.0352 (14)
$^{186}W^{32}S$	559.1392 (11)	-1.41408 (35)	-0.004 (1)[b]	0.1448255 (69)	-0.5599 (20)	-0.0335 (18)
	Mass-Scaling Relative to $^{184}W^{32}S$					
$^{182}W^{32}S$	0.999991	1.000000[a]	1.000000[a]	1.000125	1.036	1.111
$^{183}W^{32}S$	0.999994	1.000000[a]	1.000000[a]	1.000006	1.087	0.718
$^{186}W^{32}S$	1.000013	1.000000[a]	1.000000[a]	1.000038	1.066	0.955

[a]Line positions for the (0,2) band of the [13.10]1 – $X0^+$ transition were reported only for $^{186}W^{32}S$ by Tsang *et al.*[1] The mass-scaling relationship [Equation (2)] for Y_{20} was applied to estimate the parameter for the 3 other isotopologues. This mass-scaling approximation was included as a constraint in the PGOPHER[9] fit. Similar mass scaling was applied to the Y_{30} parameter.

[b]Estimated using stepwise adjustment to optimize agreement between D_0 from Ref. 6 and the D_0 value calculated from the Dunham constants with the Birge-Sponer[27] method. See Discussion for full description.

Table 2: Obtained molecular constants for v=1 of the [13.10] Ω=1 state of WS. All values are reported in cm^{-1}.

	[13.10] Ω=1 State			
	v=1			
	T_1[a]	B_1	$D_1 \times 10^6$	$H_1 \times 10^{12}$
$^{182}W^{32}S$	13813.08891 (79)	0.1374412 (76)	0.0458 (30)	-21.06 (35)
$^{183}W^{32}S$	13812.8075 (10)	0.1373104 (88)	0.0453 (42)	-18.13 (59)
$^{184}W^{32}S$	13812.53598 (75)	0.1372002 (59)	0.0358 (22)	-22.75 (29)
$^{186}W^{32}S$	13812.0084 (11)	0.1369530 (74)	0.0269 (28)	-24.29 (38)
	$q \times 10^3$	$q_D \times 10^6$	$q_H \times 10^9$	
$^{182}W^{32}S$	0.0394 (28)	-0.0243 (26)	0.03432 (58)	
$^{183}W^{32}S$	0.0369 (38)	-0.0185 (39)	0.03206 (96)	
$^{184}W^{32}S$	0.0379 (26)	-0.0232 (23)	0.03432 (49)	
$^{186}W^{32}S$	0.0398 (29)	-0.0240 (27)	0.03443 (59)	

[a]The minimum of the Dunham potential was set to zero in the fit. As such, these excitation energies include the zero-point energy of each isotopologue.

Table 3: Root mean squared (RMS) residuals for the fit of the (1,0) band of the [13.10] Ω=1 – $X\,^3\Sigma^-_{0^+}$ transition of WS. Resolved lines were assigned an experimental uncertainty of 0.003 cm^{-1}, consistent with the RMS values from the PGOPHER[9] fit.

	ILS-FTS			
	N	**RMS (cm^{-1})**	**Deweighted Lines[a]**	**RMS for Resolved Lines (cm^{-1})**
$^{182}W^{32}S$	167	0.0027	19	0.0026
$^{183}W^{32}S$	150	0.0042	57	0.0038
$^{184}W^{32}S$	178	0.0047	34	0.0035
$^{186}W^{32}S$	160	0.0041	40	0.0032
Total	655	0.0039	150	0.0032

	LIF[b]	
	N	**RMS (cm^{-1})**
Tsang *et al.*[1]	1104	0.0036

[a]Blended or obscured line positions were deweighted in the fit by a factor of three.

[b]Data reported by Tsang *et al.*[1]

Table 4: Line positions, assignments, and residuals for the fit of the (1,0) band of the [13.10] Ω=1 - $X\,^3\Sigma^-_{0^+}$ transition of WS. Blended lines are marked with an asterisk (*) and were deweighted in the fit.

	$^{182}W^{32}S$		$^{183}W^{32}S$		$^{184}W^{32}S$		$^{186}W^{32}S$	
Line Label	**Position**	**Obs-Calc**	**Position**	**Obs-Calc**	**Position**	**Obs-Calc**	**Position**	**Obs-Calc**
P(4)	*13532.1687	-0.0023			*13531.8408	-0.0040		
P(5)	*13531.8149	-0.0055			*13531.4906	-0.0041		
P(6)	*13531.4524	-0.0022			*13531.1323	0.0029		
P(7)	*13531.0720	-0.0017			*13530.7491	0.0001		
P(8)	*13530.6763	-0.0013			*13530.3503	-0.0032	*13530.0336	-0.0147
P(9)	*13530.2656	-0.0008	13530.0971	-0.0051	13529.9383	-0.0045	*13529.6284	-0.0097
P(10)	13529.8407	0.0007	*13529.6745	-0.0018	*13529.5168	-0.0002	*13529.2046	-0.0082
P(11)	13529.3992	0.0007	*13529.2231	-0.0123	*13529.0712	-0.0049	13528.7756	0.0033
P(12)	13528.9390	-0.0029	*13528.7675	-0.0118	13528.6173	-0.0026	*13528.3114	-0.0053
P(13)	13528.4692	-0.0008	*13528.3015	-0.0066	*13528.1462	-0.0025	*13527.8416	-0.0043
P(14)	13527.9815	-0.0015	13527.8186	-0.0031	*13527.6599	-0.0024	13527.3540	-0.0060
P(15)	13527.4821	0.0013	*13527.3205	0.0003	13527.1596	-0.0011	*13526.8560	-0.0029
P(16)	13526.9636	0.0002	13526.7985	-0.0049	13526.6389	-0.0051	13526.3411	-0.0016
P(17)	13526.4327	0.0019	13526.2714	-0.0001	13526.1110	-0.0011	13525.8095	-0.0019
P(18)	13525.8842	0.0011	*13525.7195	-0.0049	13525.5661	0.0011	13525.2629	-0.0020
P(19)	13525.3181	-0.0020	13525.1575	-0.0046	13525.0043	0.0015	*13524.7020	-0.0012
P(20)	13524.7415	-0.0004	13524.5796	-0.0050	13524.4266	0.0013	13524.1225	-0.0037
P(21)	13524.1469	-0.0017	*13523.9857	-0.0061	13523.8335	0.0008	13523.5331	-0.0011
P(22)	13523.5405	0.0005	13523.3802	-0.0035	13523.2268	0.0020	13522.9270	0.0001
P(23)	13522.9159	-0.0002	13522.7627	0.0023	13522.6018	0.0001	13522.3023	-0.0021
P(24)	13522.2791	0.0022	13522.1156	-0.0062	13521.9671	0.0037	13521.6664	-0.0003
P(25)	13521.6219	-0.0006	13521.4726	0.0047	13521.3106	0.0008	13521.0124	-0.0013
P(26)	13520.9549	0.0022	*13520.8004	0.0017	13520.6397	-0.0013	13520.3495	0.0040
P(27)	13520.2703	0.0026	13520.1104	-0.0037	13519.9606	0.0037	13519.6627	0.0007
P(28)	13519.5670	-0.0003	13519.4159	0.0018	13519.2598	0.0023	13518.9608	-0.0025
P(29)	13518.8491	-0.0024	13518.7059	0.0071	13518.5445	0.0018	13518.2476	-0.0016
P(30)	13518.1209	0.0004	13517.9707	0.0028	13517.8115	-0.0012	13517.5240	0.0042
P(31)	13517.3717	-0.0023	13517.2266	0.0049	13517.0671	-0.0001	13516.7727	-0.0024
P(32)	13516.6128	0.0007	13516.4610	0.0009	13516.2995	-0.0068	13516.0177	0.0027
P(33)	13515.8349	0.0002	13515.6841	0.0012	13515.5312	0.0011	*13515.2388	-0.0007
P(34)	13515.0418	0.0000	13514.8961	0.0059	13514.7406	0.0022	13514.4460	-0.0026
P(35)	13514.2360	0.0026	13514.0835	0.0016	13513.9376	0.0064	13513.6389	-0.0033
P(36)	13513.4074	-0.0021	13513.2517	-0.0063	13513.1103	0.0018	13512.8138	-0.0064
P(37)	13512.5716	0.0015	13512.4220	0.0035	13512.2628	-0.0074	13511.9874	0.0047
P(38)	13511.7164	0.0014	13511.5594	-0.0040	13511.4144	-0.0020	13511.1349	0.0053
P(39)	13510.8446	0.0004	13510.6991	0.0066	13510.5394	-0.0074	13510.2625	0.0015
P(40)	13509.9609	0.0031	13509.8018	-0.0041	*13509.6327	-0.0289	13509.3781	0.0014
P(41)	13509.0581	0.0025	13508.8982	-0.0053	*13508.7774	0.0167	13508.4788	0.0023
P(42)	13508.1371	-0.0005	13507.9901	0.0049	13507.8513	0.0074	13507.5596	-0.0011
P(43)	13507.2032	-0.0005	13507.0562	0.0050	13506.9190	0.0077	13506.6242	-0.0048
P(44)	13506.2582	0.0041	13506.1024	0.0013	13505.9643	0.0015	13505.6836	0.0023
P(45)	13505.2929	0.0045	13505.1379	0.0028	13505.0006	0.0023	13504.7195	0.0017
P(46)	13504.3118	0.0051	13504.1570	0.0040	13504.0203	0.0025	13503.7389	0.0007
P(47)	13503.3068	-0.0022	13503.1617	0.0068	13503.0239	0.0027	13502.7457	0.0033
P(48)	13502.2939	-0.0012	13502.1453	0.0046	13502.0070	-0.0014	13501.7314	0.0010
P(49)	13501.2644	-0.0008	13501.1020	-0.0082	13500.9796	0.0004	13500.7012	-0.0010
P(50)	13500.2226	0.0038			13499.9324	-0.0013	13499.6590	0.0015
P(51)	13499.1552	-0.0010			13498.8755	0.0037	13498.6050	0.0086
P(52)	13498.0776	0.0005			13497.7931	-0.0001	13497.5166	-0.0021
P(53)	13496.9813	-0.0002			13496.6964	-0.0017	13496.4232	-0.0012
P(54)					13495.5899	0.0038	13495.3160	0.0028
P(55)					13494.4618	0.0045	13494.1865	0.0014
P(56)					13493.3142	0.0027	13493.0429	0.0030
P(57)					13492.1473	-0.0012		
P(58)					13490.9673	-0.0009		
P(59)					13489.7735	0.0029		
P(60)					13488.5563	0.0009		

Table 4 (continued)

	$^{182}W^{32}S$		$^{183}W^{32}S$		$^{184}W^{32}S$		$^{186}W^{32}S$	
Line Label	**Position**	**Obs-Calc**	**Position**	**Obs-Calc**	**Position**	**Obs-Calc**	**Position**	**Obs-Calc**
Q(1)	*13533.4050	-0.0019	13533.2351	-0.0037				
Q(2)	*13533.3778	0.0014	*13533.2069	-0.0016	13533.0431	-0.0052		
Q(3)	*13533.3287	-0.0020	13533.1648	0.0019	*13532.9988	-0.0038		
Q(4)	13533.2670	-0.0029	*13533.1024	0.0002	13532.9404	-0.0014		
Q(5)	13533.1913	-0.0025	13533.0255	-0.0008	13532.8579	-0.0078		
Q(6)	13533.1025	0.0000	*13532.9339	-0.0013	13532.7728	-0.0016		
Q(7)	*13532.9954	-0.0005	*13532.8277	-0.0012	13532.6671	-0.0009	*13532.3704	0.0118
Q(8)	13532.8709	-0.0032	13532.7082	0.0008	13532.5461	-0.0002	*13532.2433	0.0065
Q(9)	13532.7384	0.0013	13532.5780	0.0073	13532.4081	-0.0013	13532.1046	0.0046
Q(10)	13532.5867	0.0018	*13532.4206	0.0018	13532.2586	0.0013	13531.9513	0.0036
Q(11)	13532.4153	-0.0022	*13532.2513	-0.0004	13532.0939	0.0040	13531.7847	0.0044
Q(12)	*13532.2356	0.0008	13532.0706	0.0012	13531.9103	0.0029	13531.5981	0.0004
Q(13)	13532.0382	0.0013	*13531.8657	-0.0062	13531.7117	0.0020	13531.4015	0.0016
Q(14)	13531.8271	0.0034	13531.6604	0.0013	13531.4999	0.0032	13531.1842	-0.0026
Q(15)	13531.6008	0.0055	13531.4333	0.0022	13531.2717	0.0033	13530.9611	0.0025
Q(16)	13531.3556	0.0040	*13531.1916	0.0038	13531.0276	0.0027	13530.7174	0.0024
Q(17)	13531.0959	0.0033	13530.9357	0.0065	13530.7700	0.0039	13530.4603	0.0040
Q(18)	*13530.8203	0.0020	*13530.6592	0.0040	13530.4971	0.0050	13530.1860	0.0038
Q(19)	13530.5322	0.0036	13530.3676	0.0016	13530.2072	0.0044	*13529.8956	0.0027
Q(20)	13530.2283	0.0046	13530.0627	0.0014	*13529.9047	0.0066	*13529.5911	0.0029
Q(21)	*13529.9048	0.0015	13529.7421	0.0009	13529.5780	0.0000	13529.2719	0.0037
Q(22)	13529.5699	0.0025	13529.4071	0.0014	13529.2487	0.0061	13528.9372	0.0045
Q(23)	13529.2187	0.0026	13529.0545	-0.0001	13528.8958	0.0042	13528.5847	0.0028
Q(24)	13528.8524	0.0031	13528.6893	0.0012	13528.5291	0.0039	13528.2206	0.0050
Q(25)	13528.4691	0.0023	*13528.3030	-0.0028	13528.1471	0.0039	13527.8381	0.0044
Q(26)	13528.0723	0.0035	*13527.9084	0.0005	13527.7505	0.0049	13527.4388	0.0026
Q(27)	13527.6572	0.0023	13527.4922	-0.0019	13527.3346	0.0023	13527.0253	0.0022
Q(28)	13527.2265	0.0012	*13527.0674	0.0028	13526.9050	0.0019	13526.5974	0.0032
Q(29)	13526.7794	-0.0002	13526.6178	-0.0012	13526.4594	0.0012	*13526.1518	0.0024
Q(30)	13526.3172	-0.0008	*13526.1518	-0.0056	13525.9984	0.0013	*13525.6903	0.0017
Q(31)	13525.8396	-0.0007	*13525.6778	-0.0018	13525.5180	-0.0019	13525.2110	-0.0007
Q(32)	13525.3443	-0.0019	13525.1803	-0.0052	13525.0244	-0.0021	13524.7161	-0.0025
Q(33)	13524.8333	-0.0024	13524.6741	-0.0008	13524.5150	-0.0017	13524.2093	0.0002
Q(34)	13524.3057	-0.0028	*13524.1409	-0.0067	13523.9856	-0.0046	13523.6792	-0.0039
Q(35)	13523.7602	-0.0045	*13523.6065	0.0029	13523.4415	-0.0056	13523.1360	-0.0043
Q(36)	13523.2002	-0.0037	13523.0405	-0.0021	13522.8805	-0.0064	13522.5773	-0.0033
Q(37)	13522.6227	-0.0032	13522.4625	-0.0020	13522.3015	-0.0081	13521.9993	-0.0045
Q(38)	13522.0265	-0.0040	13521.8645	-0.0044	13521.7052	-0.0098	*13521.4032	-0.0063
Q(39)	*13521.4129	-0.0046	13521.2566	0.0008	*13521.0898	-0.0129	*13520.7908	-0.0069
Q(40)	*13520.7820	-0.0045	13520.6249	0.0002	*13520.4656	-0.0068	13520.1627	-0.0052
Q(41)	13520.1328	-0.0047	13519.9713	-0.0042	*13519.8291	0.0052	13519.5140	-0.0059
Q(42)	13519.4675	-0.0023	13519.3092	0.0014	13519.1577	0.0008	13518.8492	-0.0043
Q(43)	13518.7814	-0.0019	13518.6239	0.0025	13518.4690	-0.0020	13518.1634	-0.0046
Q(44)	13518.0765	-0.0011	13517.9167	0.0008	13517.7648	-0.0010	13517.4598	-0.0035
Q(45)	13517.3528	0.0005	13517.1969	0.0060	13517.0389	-0.0022	13516.7358	-0.0032
Q(46)	13516.6079	0.0008	13516.4541	0.0080	13516.2997	0.0035	13515.9940	-0.0006
Q(47)	13515.8390	-0.0023	13515.6842	0.0032	13515.5312	0.0004	13515.2322	0.0026
Q(48)	13515.0582	0.0035	13514.8961	0.0009	13514.7406	-0.0037	13514.4459	0.0024
Q(49)	13514.2510	0.0043	13514.0829	-0.0054	13513.9373	0.0009	13513.6388	0.0029
Q(50)	13513.4164	-0.0003	13513.2530	-0.0067	13513.1103	0.0039	13512.8138	0.0077
Q(51)	13512.5700	0.0058	13512.4106	0.0017	*13512.2627	0.0090	13511.9573	0.0038
Q(52)	13511.6915	0.0029	13511.5316	-0.0039	13511.3856	0.0079	13511.0823	0.0047
Q(53)	13510.7932	0.0039	13510.6433	0.0047	13510.4832	0.0055	13510.1822	0.0046
Q(54)	13509.8700	0.0045	13509.7165	-0.0013	13509.5573	0.0041	13509.2525	-0.0003
Q(55)	13508.9178	0.0012			*13508.6072	0.0040	13508.3056	0.0031
Q(56)	13507.9383	-0.0034			13507.6303	0.0032	13507.3300	0.0043
Q(57)	13506.9377	-0.0026			13506.6241	0.0002	13506.3186	-0.0033
Q(58)	13505.9065	-0.0047			13505.5873	-0.0056	13505.2868	-0.0032
Q(59)					13504.5271	-0.0060	13504.2227	-0.0063

Table 4 (continued)

	$^{182}W^{32}S$		$^{183}W^{32}S$		$^{184}W^{32}S$		$^{186}W^{32}S$	
Line Label	**Position**	**Obs-Calc**	**Position**	**Obs-Calc**	**Position**	**Obs-Calc**	**Position**	**Obs-Calc**
R(0)	13533.6948	-0.0022			13533.3629	-0.0055	13533.0521	-0.0066
R(1)	13533.9535	-0.0033			13533.6236	-0.0041	13533.3215	0.0040
R(2)	13534.1969	-0.0045	*13534.0377	0.0050	13533.8709	-0.0009	13533.5562	-0.0050
R(3)	13534.4315	0.0006	13534.2651	0.0031	13534.0985	-0.0024	13533.7885	-0.0013
R(4)	13534.6434	-0.0018	13534.4732	-0.0030	13534.3190	0.0042	*13533.9978	-0.0053
R(5)	13534.8431	-0.0013	*13534.6732	-0.0021	13534.5108	-0.0026	*13534.1924	-0.0090
R(6)	13535.0266	-0.0019	*13534.8578	-0.0015	*13534.6867	-0.0103	*13534.3785	-0.0060
R(7)	13535.1978	0.0005	*13535.0266	-0.0015	*13534.8606	-0.0049	*13534.5462	-0.0063
R(8)	13535.3486	-0.0024	*13535.1833	0.0016	13535.0206	0.0019	*13534.6986	-0.0066
R(9)	13535.4879	-0.0016	*13535.3181	-0.0021	13535.1601	0.0033	*13534.8360	-0.0069
R(10)	13535.6122	-0.0006	13535.4433	-0.0004	13535.2804	0.0007	*13534.9706	0.0052
R(11)	13535.7247	0.0037	*13535.5502	-0.0016	*13535.3926	0.0051	*13535.0658	-0.0069
R(12)	13535.8183	0.0044	*13535.6446	-0.0003	13535.4817	0.0015	*13535.1577	-0.0071
R(13)	13535.8881	-0.0036	*13535.7236	0.0008	13535.5561	-0.0015	*13535.2346	-0.0072
R(14)	13535.9580	0.0037	13535.7884	0.0029	13535.6198	0.0000	*13535.2963	-0.0072
R(15)	13536.0063	0.0047	*13535.8332	0.0003	13535.6635	-0.0033	*13535.3430	-0.0072
R(16)	13536.0389	0.0052	*13535.8639	-0.0012	*13535.7009	0.0022	*13535.3744	-0.0072
R(17)	13536.0491	-0.0015	13535.8866	0.0045	*13535.7171	0.0018	*13535.3929	-0.0049
R(18)	13536.0475	-0.0047	*13535.8866	0.0027	*13535.7181	0.0014	*13535.3929	-0.0059
R(19)	13536.0365	-0.0020	*13535.8702	-0.0002	*13535.7038	0.0010	*13535.3780	-0.0066
R(20)	13536.0053	-0.0043	*13535.8443	0.0027	13535.6755	0.0017	*13535.3489	-0.0063
R(21)	13535.9678	0.0024	13535.8040	0.0064	13535.6321	0.0026	*13535.3045	-0.0059
R(22)	13535.9035	-0.0024	*13535.7376	-0.0006	13535.5706	0.0008	13535.2496	-0.0009
R(23)	13535.8322	0.0012	*13535.6661	0.0027	13535.4987	0.0038	*13535.1760	0.0008
R(24)	13535.7381	-0.0028	*13535.5748	0.0014	13535.4017	-0.0030	13535.0831	-0.0016
R(25)	13535.6321	-0.0031	13535.4653	-0.0026	13535.3022	0.0030	13534.9790	0.0001
R(26)	13535.5107	-0.0037	*13535.3491	0.0020	13535.1761	-0.0022	13534.8580	0.0003
R(27)	13535.3784	0.0004	13535.2099	-0.0008	13535.0410	-0.0010	*13534.7206	-0.0006
R(28)	13535.2288	0.0025	13535.0535	-0.0055	13534.8900	-0.0004	13534.5692	-0.0001
R(29)	13535.0594	0.0004	*13534.8841	-0.0076	13534.7210	-0.0023	13534.4017	-0.0004
R(30)	13534.8800	0.0037	*13534.7052	-0.0038	13534.5420	0.0011	13534.2203	0.0010
R(31)	13534.6790	0.0009	*13534.5108	0.0000	13534.3437	0.0008	13534.0221	0.0010
R(32)	13534.4624	-0.0019	13534.2958	-0.0011	13534.1270	-0.0024	13533.8117	0.0042
R(33)	13534.2370	0.0020	13534.0676	0.0001	13533.8996	-0.0008	13533.5790	0.0007
R(34)	13533.9888	-0.0013	*13533.8182	-0.0041	13533.6548	-0.0010	13533.3341	0.0006
R(35)	13533.7283	-0.0012	13533.5645	0.0029	13533.3930	-0.0025	13533.0729	-0.0004
R(36)	13533.4552	0.0019	13533.2815	-0.0036	13533.1162	-0.0035	13532.7985	0.0012
R(37)	13533.1581	-0.0032	*13532.9937	0.0008	13532.8195	-0.0086	13532.5043	-0.0013
R(38)	*13532.8464	-0.0071	13532.6835	-0.0014	*13532.5087	-0.0121	13532.2024	0.0042
R(39)	13532.5299	0.0000	13532.3551	-0.0060	*13532.1966	-0.0011	13531.8747	-0.0004
R(40)	13532.1869	-0.0036	13532.0181	-0.0033	*13531.8701	0.0115	13531.5351	-0.0009
R(41)	13531.8322	-0.0030	*13531.6640	-0.0017	13531.5063	0.0026	*13531.1820	0.0010
R(42)	13531.4632	-0.0007	13531.2925	-0.0016	13531.1323	-0.0005	*13530.8109	0.0008
R(43)	13531.0743	-0.0022	13530.9054	-0.0010	13530.7492	0.0034	13530.4216	-0.0015
R(44)	13530.6716	-0.0015	*13530.4975	-0.0052	13530.3425	-0.0003	13530.0180	-0.0020
R(45)	13530.2531	-0.0005	13530.0811	-0.0017	*13529.9146	-0.0089	*13529.6008	0.0001
R(46)	13529.8170	-0.0007	*13529.6444	-0.0024	13529.4845	-0.0034	13529.1647	-0.0005
R(47)	13529.3632	-0.0024	*13529.1800	-0.0146	13529.0362	0.0002	13528.7102	-0.0031
R(48)	*13528.8952	-0.0020	*13528.7165	-0.0093	13528.5659	-0.0017	13528.2478	0.0030
R(49)	13528.4119	-0.0004	*13528.2262	-0.0147	*13528.0784	-0.0042	*13527.7580	-0.0019
R(50)	13527.9101	-0.0008	*13527.7349	-0.0046	*13527.5823	0.0012	13527.2572	-0.0011
R(51)	13527.3936	0.0007	*13527.2183	-0.0032	13527.0627	-0.0001	13526.7383	-0.0016
R(52)	*13526.8585	0.0004	13526.6882	0.0012	13526.5244	-0.0033	13526.2005	-0.0041
R(53)	13526.3025	-0.0041	*13526.1408	0.0050	13525.9740	-0.0015	13525.6491	-0.0033
R(54)	*13525.7341	-0.0041	*13525.5660	-0.0018	13525.4025	-0.0037	13525.0773	-0.0056
R(55)	13525.1563	0.0034	13524.9825	-0.0006	*13524.8184	-0.0014	13524.4948	-0.0014
R(56)	13524.5500	-0.0003	13524.3825	0.0011	13524.2092	-0.0067	13523.8898	-0.0022
R(57)	13523.9346	0.0040			13523.5953	0.0007	13523.2659	-0.0045
R(58)	13523.2905	-0.0031			13522.9554	-0.0002	*13522.6322	0.0012
R(59)					*13522.2940	-0.0048	*13521.9672	-0.0065
R(60)					*13521.6221	-0.0020	13521.3038	0.0056
R(61)					13520.9317	0.0005	13520.6063	0.0016
R(62)					13520.2208	0.0009		

implemented using a program provided by J. Tellinghuisen. [25] It was found (unsurprisingly) that the two vibrational parameters Y_{10} and Y_{20} were insufficient for accurate prediction of the dissociation energy, D_0, which was measured experimentally by Sevy *et al.*[6] A third vibrational parameter, Y_{30} was estimated in order to obtain better agreement between the Dunham potential and the "real" potential energy surface of WS. The corresponding Y_{30} values for the other isotopologues of WS were again constrained to equation (2). The RKR turning points for the potential are provided in Table S3. A full description of the estimation process is provided in the Discussion.

Discussion

Comparison to Computed States

The obtained molecular constants can be used to evaluate the high-level *ab initio* calculations performed by Tsang *et al.*[1] The Λ-S states obtained using the MRCISD+Q method are reported according to their relative energies, which are indicated by a number in square brackets (i.e., the $X\ ^3\Sigma^-$ state correlates to the *ab initio* [1] $^3\Sigma^-$ state). The spin-orbit interactions of these Λ-S states are estimated using the state-interaction method, producing Hund's case (c) Ω-states that are also reported according to their relative energies, indicated by a number in curly brackets (i.e., the $X\ ^3\Sigma^-_0+$ state correlates to the *ab initio* {1} 0^+ state). The electronic configurations that contribute to the Λ-S states and the Λ-S states that contribute to the Ω-states are reported in their Supplementary Materials. Our Dunham[10] analysis provides a means of direct comparison to these computed data through the determined equilibrium parameters for $^{184}W^{32}S$.

The ground state equilibrium bond length (r_e) of 2.0656 Å, though slightly shorter, compares favorably with the 2.074 Å bond length for the computed {1} 0^+ state.[1] There is also excellent agreement between the experimental (559.59 cm^{-1}) and predicted (554 cm^{-1}) ω_e values, although the anharmonicity correction $\omega_e x_e$ is overpredicted by roughly 100% (1.4 cm^{-1} vs. 3.4 cm^{-1}). These suggest that the WS bond in the $X\ ^3\Sigma^-_{0^+}$ state is slightly stronger than expected using this *ab initio* method.[1] The computed {1} 0^+ state is derived from several Λ-S states due to the large spin-orbit coupling constant of W. The computed [1] $^3\Sigma^-$ state is the dominant contributor at 67%, with a much smaller contribution from the [1] $^1\Sigma^+$ state (16%), and the remaining 27% from a mixture of other states contributing <10% each. The r_e, ω_e, and $\omega_e x_e$ values for the [1] $^3\Sigma^-$ state are 2.068 Å, 570 cm^{-1}, and 2.4 cm^{-1}, in slightly better agreement with the experimental values parameters than those of the {1} 0^+ state. The other triplet and quintet Λ-S states that make minor contributions to the {1} 0^+ state are characterized by longer bond lengths (r_e>2.1 Å) and smaller vibrational constants (ω_e<535 cm^{-1}). The experimental equilibrium parameters would seem to suggest that the $X\ ^3\Sigma^-_{0^+}$ ground state of WS has more $^3\Sigma^-$ character than predicted by Tsang *et al.*,[1] a somewhat confusing result as the large separation between the $X\ ^3\Sigma^-_{0^+}$ and $X\ ^3\Sigma^-_1$ states (2181 cm^{-1})[7,8] suggests a significant contribution from a state with Λ>0 due to its similarity to the spin-orbit constant for atomic W (2432 cm^{-1} for $5d^4$).

The WS bond in the [13.10] Ω=1 state is significantly weaker than in the $X\ ^3\Sigma^-_{0^+}$ state – its r_0 value[1] (2.1171 Å) is 2.4% longer than the ground state r_0 and the excited state $\Delta G_{1/2}$ (431 cm^{-1}) is only 77% of the ground state value. The decreased strength of this bond is further evidenced by the large number of centrifugal distortion parameters (Table 2) required to accurately describe v=1 for this electronic state. The [13.10] Ω=1 state was correlated to the *ab initio* {7} 1 state by Tsang *et al.*[1] This computed state is derived from at least 5 different Λ-S states. The predicted molecular

constants are 2.107 Å, 542 cm^{-1}, and 6.2 cm^{-1} for r_e, ω_e, and $\omega_e x_e$. While the experimental r_0 value[1] agrees reasonably well with the predicted bond length, the experimental $\Delta G_{1/2}$ value is 81% of the theoretical value of 530 cm^{-1}. The [13.10] Ω=1 state likely has a complex potential surface due to its multi-configurational origin. The difference between the experimental and *ab initio* vibrational frequencies could be due to variations in the relative Λ-S contributions. The [1] $^3\Delta$ state (ω_e 549 cm^{-1}) is the predominant contributor (56%) to the {7}1 state, with minor contributions from the [2] $^3\Pi$ state (ω_e 519 cm^{-1}; 16%), [1] $^1\Pi$ state (ω_e 540 cm^{-1}; 11%), and at least two other Λ-S states that contribute <10% (and are not specified). Of the Λ-S states within ±2000 cm^{-1} of the experimental T_0, only the [1] $^5\Delta$ state has a vibrational frequency that approaches the experimental value (T_e 13821 cm^{-1}; ω_e 483 cm^{-1}; r_e 2.162 Å). A more significant contribution from this Λ-S state would bring the *ab initio* {7} 1 state in closer alignment with the experimental [13.10] Ω=1 state.

The vibrational discrepancy could also be rationalized through interactions with energetically neighboring Ω-states. A downward shift in the T_1 value for the [13.10] Ω=1 state would result in an uncharacteristically small $\Delta G_{1/2}$ value, and the only *ab initio* states predicted to have such a low vibrational frequency lie more than 20000 cm^{-1} above the ground state. Interestingly, a heterogenous perturbation is observed in the Q(40) line of $^{184}W^{32}S$ in the ILS-FTS spectrum, as shown in Figure 4, providing firm evidence of interactions with a nearby electronic state. Clearly, the potential surface of the [13.10] Ω=1 state is indeed complex, and additional vibrational bands must be characterized to understand its nature.

Potential Energy Diagram for the X $^3\Sigma^-_{0^+}$ State of WS

The Dunham constants determined in the comprehensive fit were used to generate a potential energy surface for the *X* $^3\Sigma^-$ ground state of tungsten sulfide. The Rydberg-Kline-Rees (RKR) method was used to generate the turning points of the curve, implemented using a program provided by J. Tellinghuisen.[25] The vibrational energies were calculated using the Dunham parameters for $^{186}W^{32}S$ that were determined in this study. The potential energy curve is provided in Figure 5 and is annotated with a visual summary of the spectroscopic investigations of WS.[1,6-8]

Three vibrational levels of the *X* $^3\Sigma^-_{0^+}$ ground state have been rotationally analyzed (v=0-2). Correspondingly, two vibrational Dunham parameters can be determined from this experimental data: Y_{10} and Y_{20}, which correspond to the conventional terms ω_e and $-\omega_e x_e$. These terms can be used to estimate the equilibrium dissociation energy (also D_e, not to be confused with the centrifugal distortion constant) assuming a Morse potential.[23,26] One should always be cautious when extrapolating beyond the limits of a model. Fortunately, the dissociation energy ($D_0 \equiv D_e - G_0$) for $^{186}W^{32}S$ was measured by Sevy *et al.*[6] to be 39,800±25 cm^{-1}. Unfortunately, the D_e for the Morse potential is over 54,000 cm^{-1}, overestimated by 135% and indicating (unsurprisingly) that the Morse model does not adequately represent the ground state of WS.

To improve the correlation between the experimental observations and the analytical Dunham model, an additional vibrational parameter ($Y_{30} \approx \omega_e y_e$) was incorporated. In principle, this parameter could be estimated using the $\Delta G_{v+1/2}$ values measured by Zhang *et al.*[7] in the SVL emission experiments, observing differences in vibrational energy between v=0 and v=1-3. These measurements were incorporated into the PGOPHER[9] fit with an assigned uncertainty of ±1 cm^{-1} in accordance with the reported measurement uncertainty. The Dunham parameters determined using this approach were used to generate a potential energy surface with the RKR method, and, yet

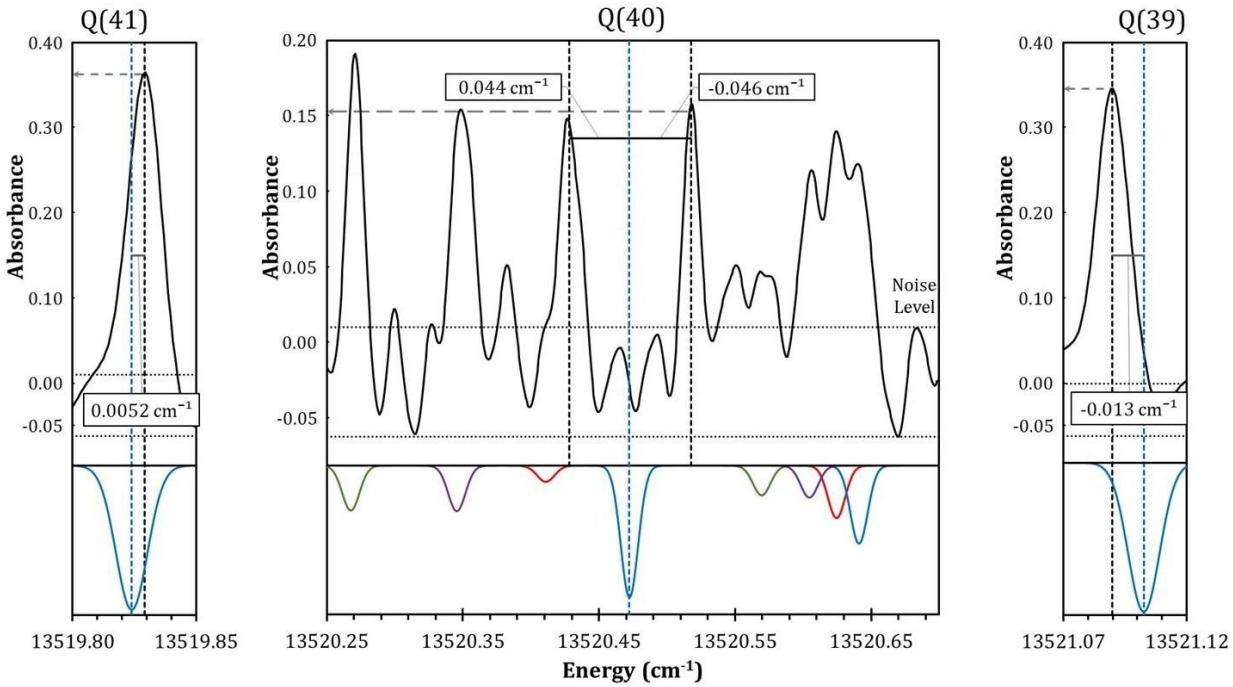

Figure 4: A heterogenous perturbation was observed in the Q-branch of the (1,0) band of the [13.10] Ω=1 – $X\,^3\Sigma^-_0{}^+$ transition of $^{184}W^{32}S$. The maximum deviation from the PGOPHER[9] simulation (shown in the lower trace) occurs at the Q(40) line, which is split into two components of equal intensity. The PGOPHER[9] simulation includes the transitions for $^{182}W^{32}S$ (green), $^{183}W^{32}S$ (red), $^{184}W^{32}S$ (blue), and $^{186}W^{32}S$ (purple), The residuals of the fit (obs-calc) are noted in the outlined boxes. The noise limits are indicated with dotted lines. The peak heights of the Q-lines of $^{184}W^{32}S$ are indicated by dashed arrows. Note that Q(39) and Q(41) lines are twice the intensity of the two features of the Q(40) transition.

again, extrapolation failed to predict the experimental dissociation energy, this time estimating a dissociation threshold near 25,000 cm^{-1}, only 63% of the measured value.

To obtain a more realistic estimate of Y_{30} and get agreement between all of the experimental studies[1,6-8] of WS, the parameter was estimated in a step-wise fashion. The relative accuracy of the estimated value was evaluated by comparing the experimental D_0 value for $^{186}W^{32}S$ to the D_0 value calculated from the vibrational Dunham parameters using the Birge-Sponer method.[23,27] The value for Y_{30} was estimated, and 5 fitting iterations were performed using PGOPHER[9] with Y_{10} and Y_{20} allowed to float and Y_{30} fixed to the estimate. The resulting vibrational Dunham parameters were used to calculate the $\Delta G_{v+1/2}$ values up to the dissociation threshold, and the values were plotted vs. (v+1/2) and fit to a 2nd order polynomial. The integral of the polynomial was calculated from v=0 to the dissociation limit (v_D), generating the estimate for D_0. Optimal agreement (within 3σ) between the two values of D_0 was obtained with an approximate Y_{30} value of -0.004 cm^{-1} (see Table 1). The $\Delta G_{v+1/2}$ values for v=0-2 calculated from the resulting Y_{10}, Y_{20}, and Y_{30} parameters of $^{184}W^{32}S$ (with Y_{20} and Y_{30} mass-scaled from the parameters for $^{186}W^{32}S$) were consistent within 3 cm^{-1} of the values reported by Zhang *et al.*[7] (also within 3σ). The optimized Dunham parameters were used to produce the RKR potential shown in Figure 5.

The resulting potential once again demonstrates the dangers of extrapolation: while the dissociation energy predicted by our Dunham model agrees with the experimentally measured value, the resulting potential energy surface deviates strongly from reality at the united-atom limit (r < 1.8 Å), where the potential flattens unrealistically allowing for inter-nuclear contact. This clear

deviation from reality underscores the limitations of simple models when dealing 5*d*-metal diatomics and our limited understanding of electronic structure of WS, which remains largely unexplored.

Conclusion

The (1,0) band of the [13.10] Ω=1 – $X\,^3\Sigma^-_{0^+}$ transition of WS has been observed and recorded at Doppler-limited resolution using intracavity laser spectroscopy detected with a Fourier-transform spectrometer (ILS-FTS). Rotational branches for $^{182}W^{32}S$, $^{183}W^{32}S$, $^{184}W^{32}S$, and $^{186}W^{32}S$ were resolved and identified. Line positions for the (0,0), (0,1), and (0,2) bands of the [13.10] Ω=1 – $X\,^3\Sigma^-_{0^+}$ and the (1,0), (1,1), (0,0), and (0,1) bands of the [12.37] Ω=1 – $X\,^3\Sigma^-_{0^+}$ transitions of WS reported by Tsang *et al.*[1] were included with the ILS-FTS data in a PGOPHER[9] fit of the data. The ground state was fit to a mass-dependent Dunham[10] model (each isotopologue treated separately) using the constrained-variables approach introduced by Brier and coauthors[11,12], and the excited states were fit band-by-band. The obtained Dunham constants were used to produce a potential energy curve for the Ω=0$^+$ component of the $^3\Sigma^-$ ground state using the RKR method.

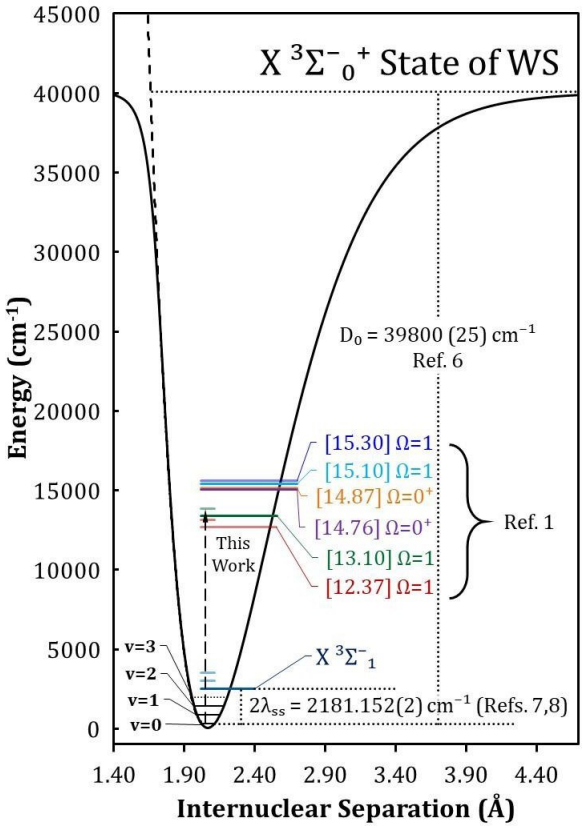

Figure 5: The RKR potential energy curve for the $X\,^3\Sigma^-_{0^+}$ state of WS is represented by the solid black line. The curve is generated from the Dunham parameters determined in this study for $^{186}W^{32}S$. Clear deviations from reality are observed near the dissociation limit, where the RKR curve curls toward the origin. The electronic states indicated by the curled bracket were rotationally analyzed from LIF spectra by Tsang *et al.*[1] The separation between the Ω-components of the $X\,^3\Sigma^-$ ground state of WS were measured with LIF and SVL emission by Zhang *et al.*[7] and ILS-FTS by our group.[8] The ground state dissociation energy, D_0 was measured by Sevy *et al.*[6] using R2PI. The numbers in brackets represent T_0 in thousands of cm^{-1} for the respective Hund's case (c) Ω-states.

Acknowledgements

This work was supported by the National Science Foundation, Grant Nos. CHE-1566454 (JOB) and CHE-1566442 (LOB).

Supplementary Materials

The Supplementary Materials contain a comparison of the band-by-band constants from Tsang *et al.*[1] and this study in Tables S1 and S2, the RKR turning points for the potential in Table S3, the ILS-FTS spectrum in text format, and the PGOPHER[9] .pgo and input files used to perform the fit. The PGOPHER[9] input file is a text file containing a linelist of the all experimental data included in this analysis, organized and labeled by experimental method, electronic transition, vibrational band, isotopologue, and rotational assignment.

References

1. L.F. Tsang, M.-C. Chan, W. Zou, A.S.-C. Cheung, *J. Mol. Spec.*, **359**, 31-36 (2019).
2. W. Zou and B. Suo, *J. Phys. Chem. A*, **120**, 6357-6370 (2016).
3. B. Grovem, M. Heyne, A.N. Mehta, H. Bender, T. Nuytten, J. Meersschaut, T. Conard, P. Verdonck, S. Van Elshocht, W. Vandervorst, S. De Gendt, M. Heyns, I. Radu, M. Caymax, and A. Delabie, *Chem. Mater.*, **29**, 2927-2938 (2017).
4. J. Park, M.S. Kim, E. Cha, J. Kim, and W. Choi, *Sci. Rep.*, **7**, 16121 (2017).
5. B. Liang and L. Andrews, *J. Phys. Chem. A*, **106**, 6945-6951 (2002).
6. A. Sevy, R.F. Huffaker, and M.D. Morse, *J. Phys. Chem. A*, **121**, 9446-9457 (2017).
7. J. Zhang, F. Fang, L. Zhang, D. Zhao, X. Ma, and J. Yang, *J. Mol. Spec.*, **366**, 111223 (2019).
8. K.N. Bales, J.C. Harms, L.C. O'Brien, and J.J. O'Brien, Talk WJ05, 74th International Symposium on Molecular Spectroscopy (2019) (http://hdl.handle.net/2142/104311). 10.15278/isms.2019.WJ05.
9. PGOPHER, A Program for Simulating Rotational, Vibrational and Electronic Spectra, C. M. Western, *JQSRT*, **186** 221-242 (2017). doi:10.1016/j.jqsrt.2016.04.010. (version 10.1.182)
10. J. L. Dunham, *Phys. Rev.*, **41**, 721 (1932).
11. A. A. Breier, B. Waßmuth, T. Büchling, G. W. Fuchs, J. Gauss, and T. F. Giesen, *J. Mol. Spec.*, **350**, 43 (2018).
12. A. A. Breier, B. Waßmuth, G. W. Fuchs, J. Gauss, and T. F. Giesen, *J. Mol. Spec.*, **355**, 46 (2019).
13. L.C. O'Brien, J.C. Harms, J.J. O'Brien, and W. Zou, *J. Mol. Struc.,* **1211**, 128024 (2020).
14. K. Kawaguchi, S. Saito, and E. Hirota, *J. Chem. Phys.*, **79**, 629-634 (1983).
15. F. Kerber, G. Nave, and C.J. Sansonetti, *ApJ*, **178**, 374-381 (2008).
16. J.C. Harms, L.C. O'Brien, and J.J. O'Brien, *J. Mol. Spec.*, **355**, 101, (2019).
17. J.C. Harms, J. Wu, S. Mian, L.C. O'Brien, and J.J. O'Brien, *J. Mol. Spec.*, **359**, 6 (2019).
18. J.C. Harms, L.C. O'Brien, and J.J. O'Brien, *J. Chem. Phys.*, **151**, 094303 (2019).
19. PGOPHER Help Website: http://pgopher.chm.bris.ac.uk/Help/variables.htm.
20. PGOPHER Help Website: http://pgopher.chm.bris.ac.uk/Help/linformat.htm.
21. J.K.G. Watson, *J. Mol. Spec.*, **80**, 411 (1980).
22. R.J. Le Roy, *J. Mol. Spec.*, **194**, 189 (1999).
23. G. Herzberg, *Molecular Spectra and Molecular Structure. I. Spectra of Diatomic Molecules* (D. Van Nostrand, Princeton, NJ, 1950).
24. P.F. Bernath, *Spectra of Atoms and Molecules*, 3rd ed., (Oxford University Press, New York, NY, 2016).
25. Personal communication with J. Tellinghuisen, Vanderbilt University.
26. P.M. Morse, *Phys. Rev.*, **34**, 57 (1929).
27. R.T. Birge and H. Sponer, *Phys. Rev.*, **28**, 259 (1926).

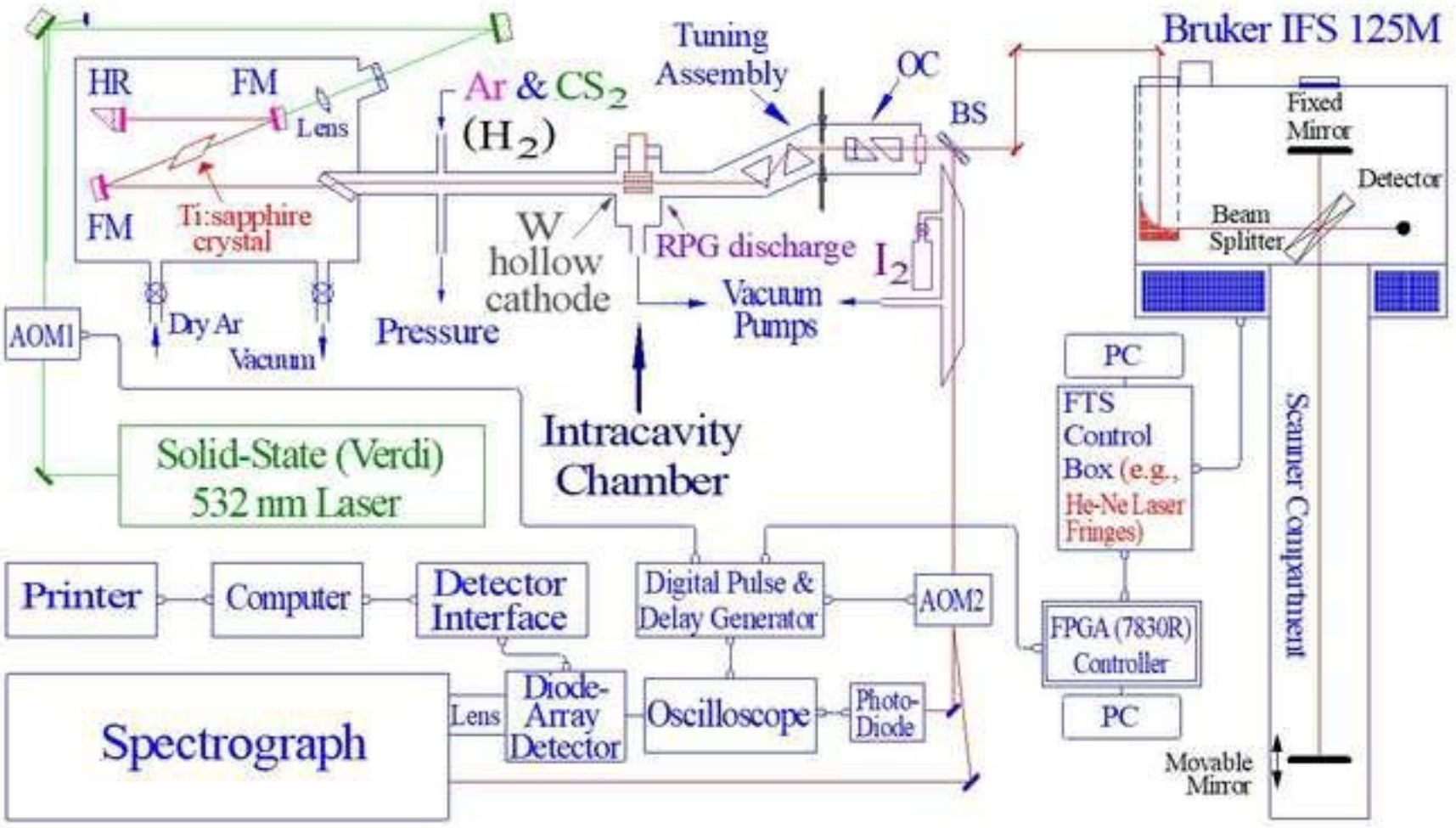
Bruker IFS 125M
Tuning Assembly
OC
BS
HR
FM
Lens
Ar & CS2
(H2)
FM
Ti:sapphire crystal
W hollow cathode
RPG discharge
I2
Fixed Mirror
Detector
Beam Splitter
AOM1
Dry Ar
Vacuum
Pressure
Vacuum Pumps
PC
FTS Control Box (e.g., He-Ne Laser Fringes)
Intracavity Chamber
Solid-State (Verdi) 532 nm Laser
Scanner Compartment
Printer
Computer
Detector Interface
Digital Pulse & Delay Generator
AOM2
FPGA (7830R) Controller
PC
Spectrograph
Lens
Diode-Array Detector
Oscilloscope
Photo-Diode
Movable Mirror

Figure 2

Click here to access/download;Figure;Figure 2_WS Spectrum with PGOPHER Simulation.jpg

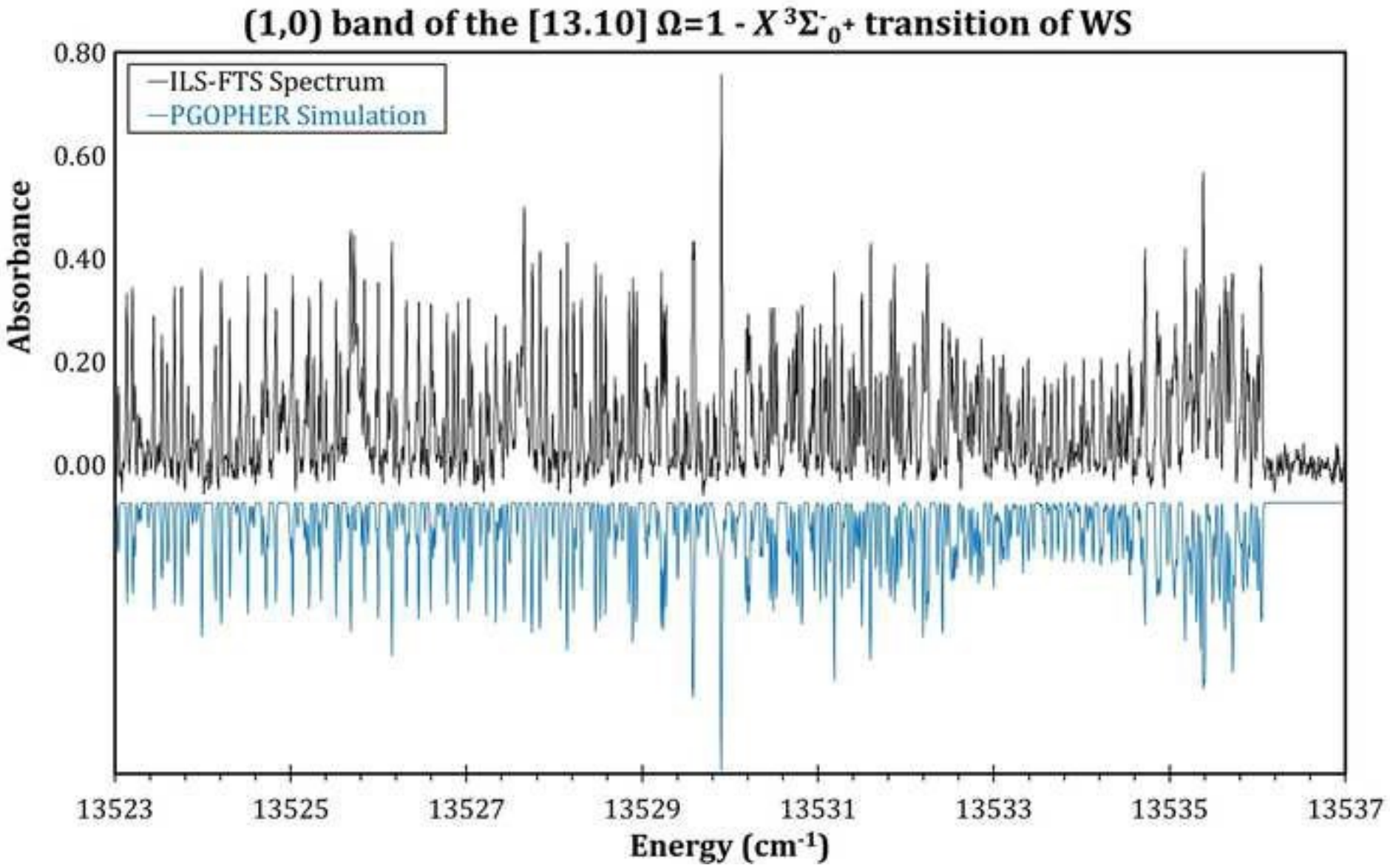

Figure 3

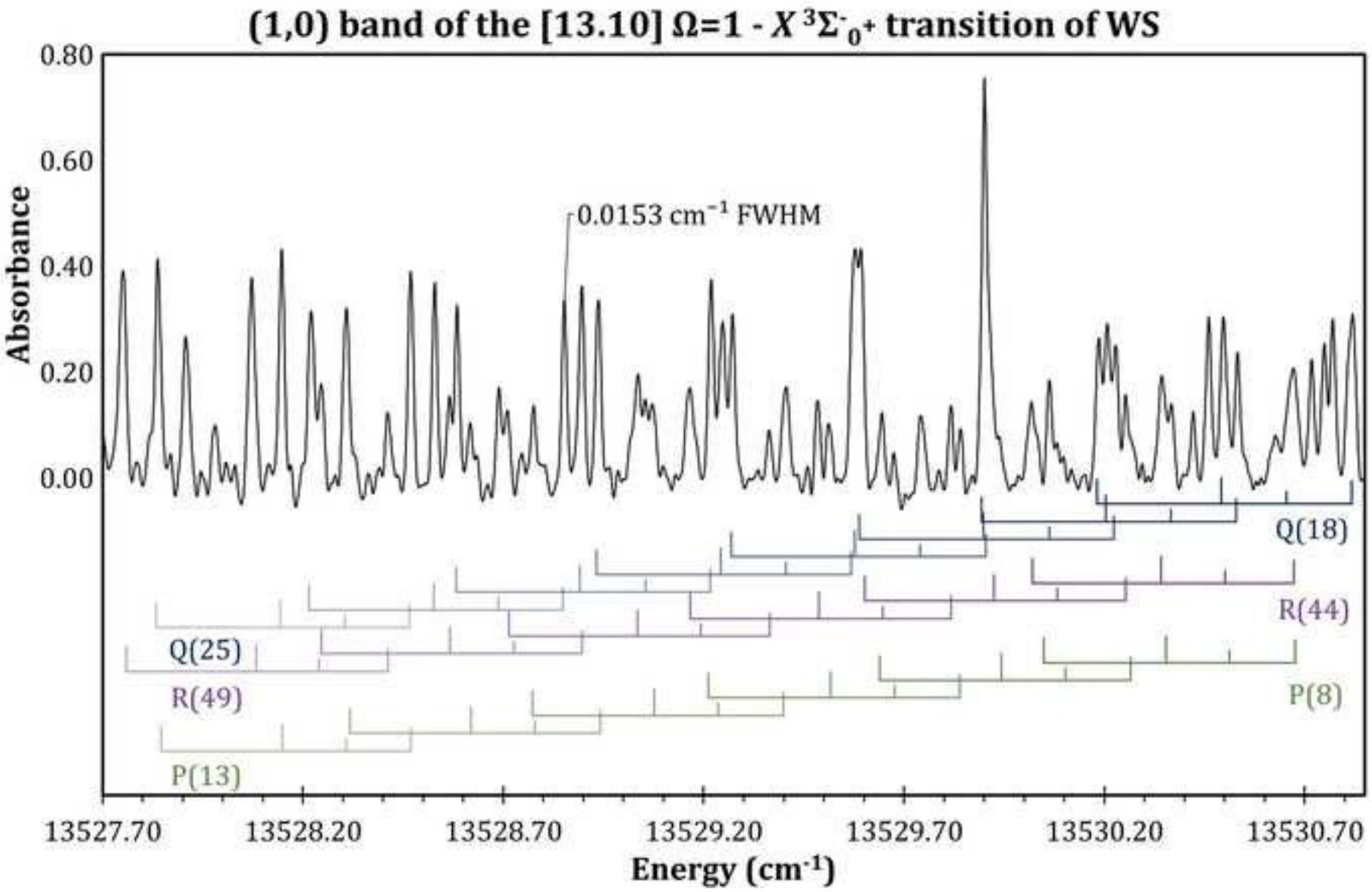

Figure 4

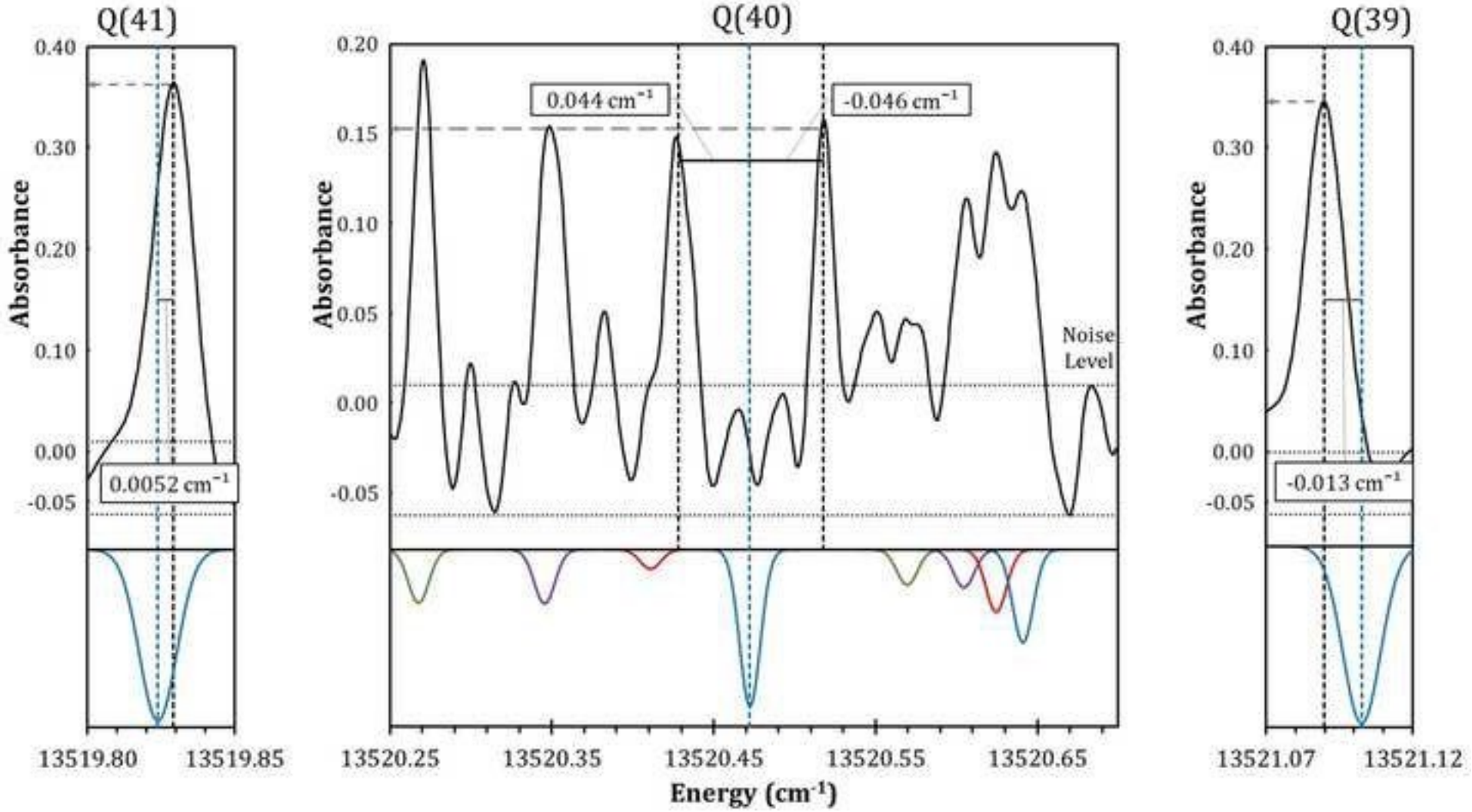

Figure 5

Click here to access/download;Figure;Figure 5 New Energy Curve.jpg

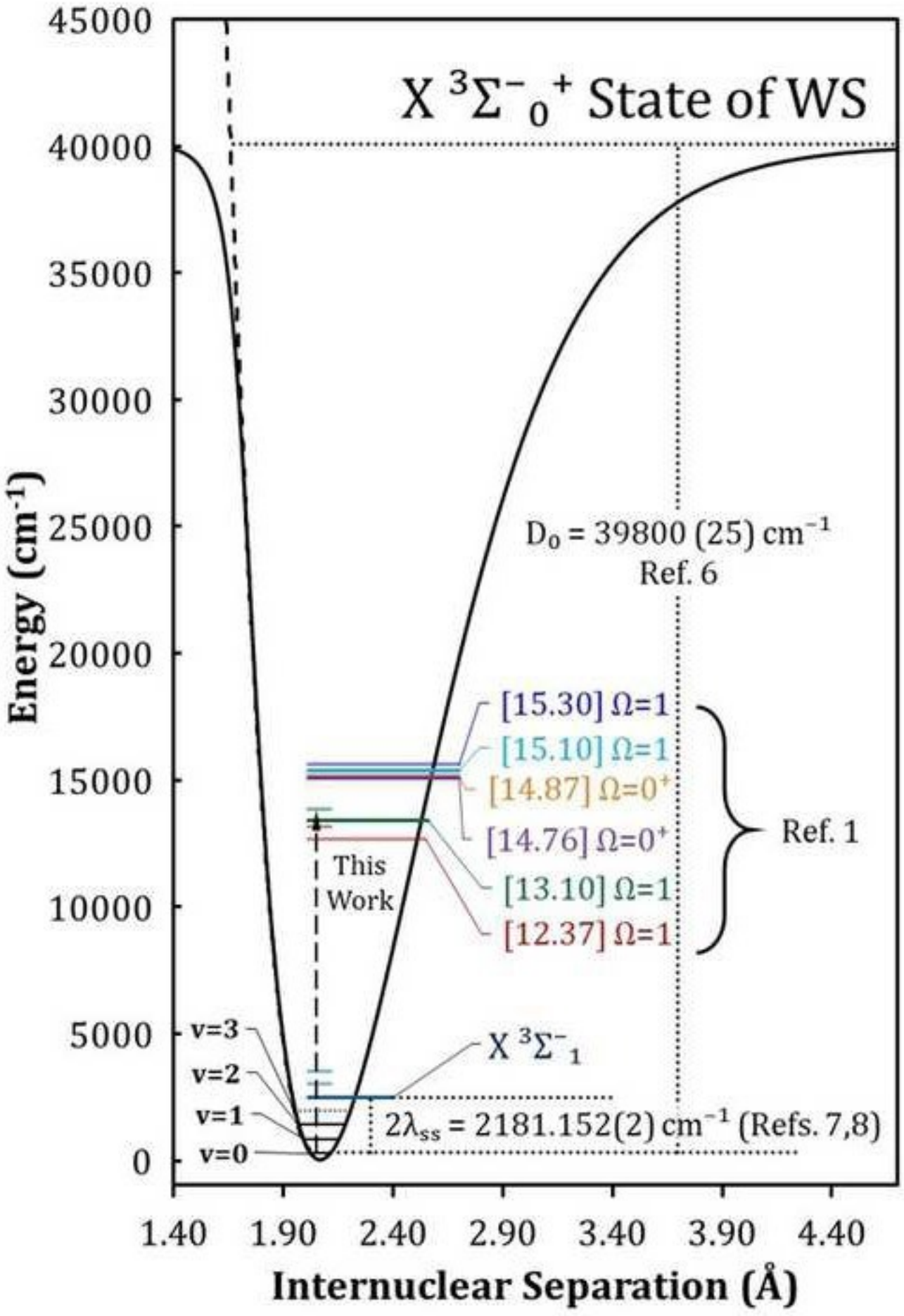

Conflict of Interest Statement

Intracavity Laser Spectroscopy with Fourier-Transform Detection of Tungsten Sulfide, WS: Analysis of the (1,0) band of the [13.10] Ω=1 – $X\,^3\Sigma^-_{0^+}$ transition

Jack C. Harms,[a] Brendan M. Ratay,[a] Kristin N. Bales, [a] James J. O'Brien,[a] and Leah C. O'Brien[b]

The authors have no conflict of interest regarding the research and data that are contained in this manuscript.

Author Credit Statement

JMSP-D-20-00110: Intracavity Laser Spectroscopy with Fourier-Transform Detection of Tungsten Sulfide, WS: Analysis of the (1,0) band of the [13.10] Ω=1 – $X\,^3\Sigma^-_{0^+}$ transition

Jack C. Harms, Brendan M. Ratay, Kristin N. Bales, James J. O'Brien, and Leah C. O'Brien

Jack C. Harms: Methodology, Software, Validation, Formal analysis, Investigation, Data Curation, Writing - Original Draft, Visualization

Brendan M. Ratay: Formal analysis, Investigation

Kristin N. Bales: Investigation

James J. O'Brien: Conceptualization, Software, Validation, Resources, Data Curation, Writing - Review & Editing, Visualization, Supervision, Funding acquisition

Leah C. O'Brien: Conceptualization, Methodology, Formal analysis, Resources, Writing - Review & Editing, Visualization, Project administration, Funding acquisition

Supplementary Materials #1

PGOPHER Input file

.pgo file